Research Square

Preprints are preliminary reports that have not undergone peer review.
They should not be considered conclusive, used to inform clinical practice,
or referenced by the media as validated information.

Water and Salt Transport Patterns and Controlling Factors in the Seawater Intrusion-Soil Salinization Hazard Chain along Silty Coasts

Dalu Yu
Shandong Provincial Geo-mineral Engineering Exploration Institute Shandong Provincial Bureau of Geology & Mineral Resources

Zitong Chai
First Institute of Oceanography, Ministry of Natural Resources

Chunwei Liu
Shandong Provincial Geo-mineral Engineering Exploration Institute Shandong Provincial Bureau of Geology & Mineral Resources

Yufeng Zhang
Key Lab of Marine Environmental Science and Ecology, Ministry of Education, Ocean University of China

Jie Sun
Jinan Jiyang District Government Service Center

Chen Qi
China Geological Survey Geophysical Survey Center

Songtao Wang
Shandong Provincial Geo-mineral Engineering Exploration Institute Shandong Provincial Bureau of Geology & Mineral Resources

Tengfei Fu
futengfei@fio.org.cn

First Institute of Oceanography, Ministry of Natural Resources

Research Article

Keywords: electrical resistivity tomography, muddy coast, seawater intrusion, soil salinisation, water and salt transport

Posted Date: November 12th, 2026

DOI: https://doi.org/10.21203/rs.3.rs-11113228/v1

License: This work is licensed under a Creative Commons Attribution 4.0 International License.
Read Full License

Additional Declarations: No competing interests reported.

Water and Salt Transport Patterns and Controlling Factors in the Seawater Intrusion-Soil Salinization Hazard Chain along Silty Coasts

Dalu Yu[1,4] | Zitong Chai[2] | Chunwei Liu[1,4] | Yufeng Zhang[5] | Jie Sun[3] | Chen Qi[6] | Songtao Wang[1,4] | Tengfei Fu[2*]

[1]Shandong Provincial Geo-mineral Engineering Exploration Institute (No. 801 Hydrogeological and Engineering Geological Brigade, Shandong Provincial Bureau of Geology and Mineral Resources), China | [2]Key Laboratory of Marine Geology and Metallogeny, First Institute of Oceanography, Ministry of Natural Resources, Qingdao 266061, China | [3]Jinan Jiyang District Government Service Center, Jinan, Shandong 251400, China | [4]Shandong Engineering Research Center for Environmental Protection and Remediation of Groundwater, China | [5]Key Laboratory of Marine Environmental Science and Ecology, Ministry of Education, Ocean University of China, Qingdao 266000, China | [6]China Geological Survey Geophysical Survey Center, China

Correspondence: Tengfei Fu (futengfei@fio.org.cn).

Funding: This work was supported by the Open Project Program of Shandong Engineering Research Center for Environmental Protection and Remediation of Groundwater (801KF2021-14) and the Deep Earth Probe and Mineral Resources Exploration-National Science and Technology Major Project (2024ZD1004103).

Abstract

In multilayer aquifer systems on muddy coasts, groundwater dynamics can jointly drive seawater intrusion and soil salinisation in the upper silty layer. However, their spatiotemporal linkage and responses to hydraulic-head difference and aquifer slope remain poorly quantified. Using Laizhou Bay as a prototype, we constructed a saturated tank model comprising silty layers above and below a sand layer. We varied head difference and slope, and monitored water and salt transport using time-lapse electrical resistivity tomography. Seawater preferentially advanced landward through the sand layer before salt migrated into the upper silty layer, causing soil salinisation. Increasing the hydraulic-head difference accelerated both processes and expanded their affected areas. Salinisation was quantified using dissolved-salt mass in pore water within 30 cm^3 of the upper silty layer. A greater head difference advanced transitions to higher salinisation classes, although salinisation and the landward extent of intrusion were not fully synchronous. At 0° slope, the nearshore upper layer remained non-salinised (<39.2 mg) for 36 h but exceeded 313.3 mg by 72 h, indicating extreme salinisation. At 1.5°, moderate salinisation (78.3–156.7 mg) occurred by 24 h and severe salinisation (156.7–313.3 mg) by 60 h; the peak then stabilised, with no extremely salinised zone developing within 72 h. These results reveal a hazard-chain sequence of preferential

sand-layer intrusion, cross-layer advective and dispersive transfer, and salt accumulation in the upper silty layer. Intrusion distance, the timing of salinisation-class transitions, and fixed-volume dissolved-salt mass provide complementary metrics for assessing this hazard chain under contrasting hydrogeological and coastal settings.

Keywords: electrical resistivity tomography, muddy coast, seawater intrusion, soil salinisation, water and salt transport

1. Introduction

Coastal zones are geographical interfaces connecting marine and terrestrial systems. They are among the most dynamic natural environments on Earth and offer highly favourable resource and environmental conditions. Nearly half of the world's population lives within 150 km of a coastline (Steyl et al., 2010). High population densities and intensive human activities have substantially increased freshwater demand, placing considerable pressure on groundwater resources. Combined with climate-driven sea-level rise, this growing demand has left coastal regions increasingly vulnerable to seawater intrusion and associated hazards, including soil salinisation and ecosystem degradation (Neubauer et al., 2013; Thorn and Urish, 2013; Hopfensperger et al., 2014; Vallejos et al., 2015; Xu et al., 2020). These hazards are causally interconnected and may reinforce one another, thereby forming a geohazard chain (Han et al., 2007). Seawater intrusion and soil salinisation have become major geological hazards that constrain the sustainable development of industry and agriculture in coastal regions. Severe seawater intrusion has occurred along the coasts of Laizhou Bay, Beibu Gulf, Bohai Bay and Liaodong Bay in China (Wang, 2020; Guo, 2019), posing substantial threats to regional water and soil resources and food security.

Seawater intrusion essentially results from the disruption of the hydraulic equilibrium at the coastal freshwater–seawater interface following changes in groundwater level or sea level, causing the interface to migrate landward. Research on seawater intrusion can be traced back to 1828 and has progressed through four theoretical stages: hydrostatic analysis, groundwater-flow analysis, the simultaneous treatment of flow and dispersion, and fully coupled flow–dispersion analysis. During this development, classical formulations such as the Ghyben–Herzberg relation and the advection–dispersion equation have been progressively refined (Zhang, 2021; Glover, 1959; Cooper, 1964). Previous studies have broadly followed three directions: theoretical analysis, laboratory experimentation and field monitoring. Laboratory experiments, in particular, have

progressed from simulations of single homogeneous aquifers to investigations of multilayered heterogeneous systems (Kooi et al., 2000; Stigter et al., 2014; Tong, 2015). Soil salinisation is the process by which water-soluble salts accumulate and are redistributed within weathered soil under natural and anthropogenic influences. Relevant studies have primarily examined its causes, patterns of water and salt transport, the physicochemical properties of saline soils, monitoring and assessment, and integrated remediation (Wang et al., 1993; Li, 2018; Li et al., 2022). Groundwater is a major driver of salt transport, accumulation and exchange, and both groundwater depth and mineralisation directly affect the severity of soil salinisation (Salama et al., 1999; Ibrakhimov et al., 2007; Wang et al., 2008). Common techniques for monitoring water and salt transport include point-based sampling and analysis, neutron logging, solute and isotope tracing, remote sensing, and geophysical methods. Among these, electrical resistivity tomography (ERT) has been widely used to delineate freshwater–seawater interfaces and assess soil salinisation because it enables non-destructive, continuous in situ monitoring (Yao et al., 2007; Hu and Tian, 2000; He, 2016; Kazakis, 2016; Abliz et al., 2016; Ouhamdouch et al., 2017; Oiro, 2018).

Despite this progress, three important knowledge gaps remain. First, most physical models employ homogeneous or single-aquifer configurations and therefore provide limited insight into preferential seawater intrusion through sand layers and subsequent salt transfer into overlying silty layers (Salehin et al., 2018). Second, hydrodynamic boundary conditions are commonly represented by either a single hydraulic-head difference or a change in sea level. Systematic comparisons of the responses of seawater intrusion and soil salinisation to the combined effects of hydraulic-head difference and stratal slope remain scarce (Yu et al., 2019; Ahmed et al., 2022). Third, although ERT has been used to delineate freshwater–seawater interfaces in coastal environments (Comte and Banton, 2007; Beaujean et al., 2014), relatively few studies have quantitatively converted time-lapse resistivity changes into salinity, salt storage and

salinisation severity classes (Xu et al., 2020; Qi et al., 2023).

To address these gaps, this study used the layered aquifer system along the muddy coast of Laizhou Bay as a prototype and combined theoretical analysis with laboratory tank experiments. A physical model comprising an upper silty layer, a middle sand layer and a lower silty layer was constructed under different combinations of hydraulic-head difference and stratal slope. Time-lapse ERT was then used to continuously monitor water and salt transport. Methods were developed to convert resistivity into salinity and to calculate the dissolved-salt mass within a fixed soil volume. Seawater-intrusion distance, salinity distribution and upper-layer soil-salinisation severity were used as complementary indicators to characterise a hazard-chain process involving preferential intrusion through the sand layer, interlayer salt transfer and salt accumulation in the upper silty layer. The findings provide an experimental basis for the integrated assessment of seawater intrusion and soil salinisation along muddy coasts.

2. Study area

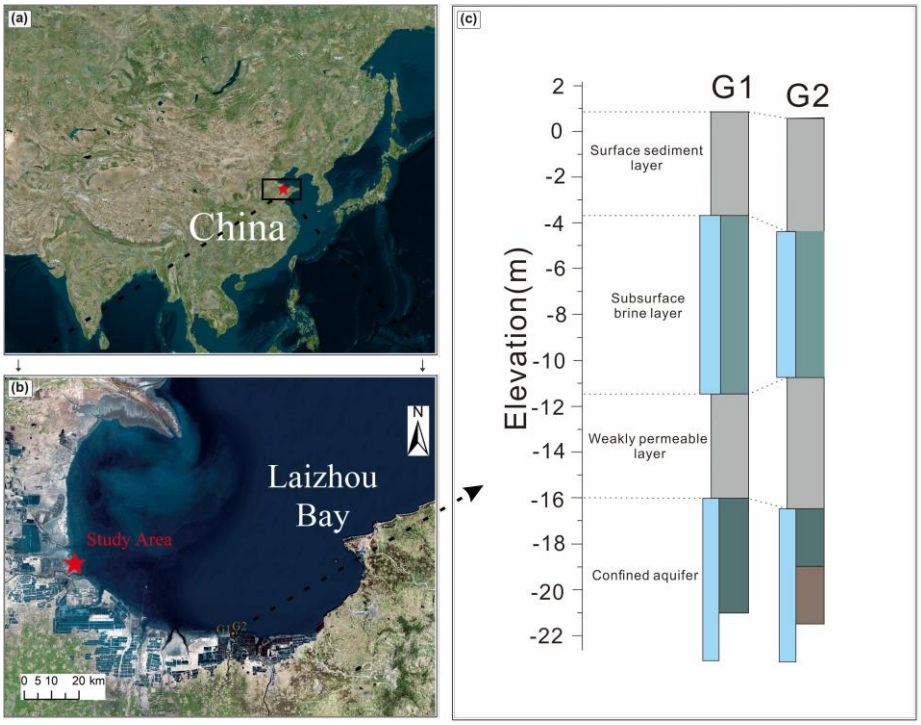


Figure 1. Location of the study area. (a, b) Location of the study area on the southwestern coast of Laizhou Bay, eastern China. (c) G1 and G2 denote two geological boreholes along the coast of Laizhou Bay. Map lines delineate study areas and do not necessarily depict accepted national boundaries.

The physical model was developed based on the hydrogeomorphological conditions of southwestern Laizhou Bay. From south to north, the region comprises three distinct geomorphological units: a piedmont alluvial–proluvial plain, an alluvial–marine plain and a coastal marine plain. The terrain generally decreases in elevation from south to north and slopes very gently from inland areas towards the sea. The nearshore zone is characterised by extensive tidal flats with gentle slopes (Gao et al., 2016; Zhang, 2025). Tidal forcing is pronounced in the study area. Tidal currents flow southwestward during flood tide and northeastward during ebb tide, with a maximum velocity of 0.5 $km \cdot h^{-1}$. The highest and lowest recorded tidal levels are 6.01 and 1.40 m, respectively (Qi, 2023). Storm-surge-induced seawater inundation is a major regional hazard. Such events occur mainly from March to April and in autumn, generally when tidal levels exceed 4~5 m.

Over the past six to seven decades, both saline and fresh groundwater along the southern coast of Laizhou Bay have been intensively exploited to meet the demands of agriculture, the underground-brine industry and local communities. Over the past 20 years, large-scale coastal underground-brine abstraction has formed several regional-scale cones of depression, resulting in pronounced fluctuations in nearshore groundwater levels. This anthropogenic disturbance has disrupted the original hydraulic equilibrium, altered both the hydraulic gradient and groundwater-flow direction, and caused the previously stable freshwater–saltwater interface to migrate markedly landward, thereby intensifying seawater intrusion (Sun et al., 2023; Zhang et al., 2025).

A complete Quaternary stratigraphic succession is developed within the study area. Fluvial–lacustrine facies predominate in the Early to Middle Pleistocene strata, with marine beds intercalated within the Middle Pleistocene sequence, whereas the Late Pleistocene to Holocene succession comprises alternating marine and continental deposits. The plain is broad and flat and has experienced three marine transgressions since the Late Pleistocene (Table 1). Three transgression–regression cycles associated with large-scale sea-level fluctuations formed three saline aquifers at depths of 5.80~18.58, 18.58~23.27 and 23.27~49.15 m, respectively (Zhang, 2025). The transgressive strata consist predominantly of relatively coarse-grained sediments, including silty to fine sand and medium-to-coarse sand, with minor clayey silt.

Table 1. Stratigraphic distribution within the upper 50 m along the southern coast of Laizhou Bay.

Geological age (ka BP)	stratum	depth (m)	Lithology
Holocene(3.2~ 11.6)	Huanghua transgression strata	5.8~18.58	silty fine sand, clayey silt
late Late Pleistocene (11.6~ 61.0)	continental strata	18.58~23.27	silty clay, clayey silt
late Late Pleistocene (11.6~ 61.0)	Xianxian transgression strata	23.27~49.15	silty fine sand, clayey silt

3. Materials and Methods

3.1 Experimental tank apparatus

The laboratory apparatus comprised two components: an experimental tank and a monitoring system. The tank system was constructed from acrylic sheets and measured 177 × 55 × 87.5 cm (length × width × height; Figure 2). Water-supply reservoirs were positioned at both ends of the apparatus and contained freshwater and saltwater, respectively. Each side reservoir measured 13.5 × 55 × 87.5 cm (length × width × height). The central main tank, measuring 150 × 55 × 87.5 cm (length × width × height), was filled with clayey soil and sand to simulate a multilayer aquifer system.

The side reservoirs were separated from the main tank by perforated acrylic partitions. Both faces of each partition were covered with fine-mesh screen and nonwoven fabric to prevent fine sediment from clogging the perforations or entering the side reservoirs. A water-level regulation unit was installed outside each side reservoir. Each unit consisted primarily of a Mariotte bottle and a variable-flow pump and was used to control the water level in the corresponding reservoir.

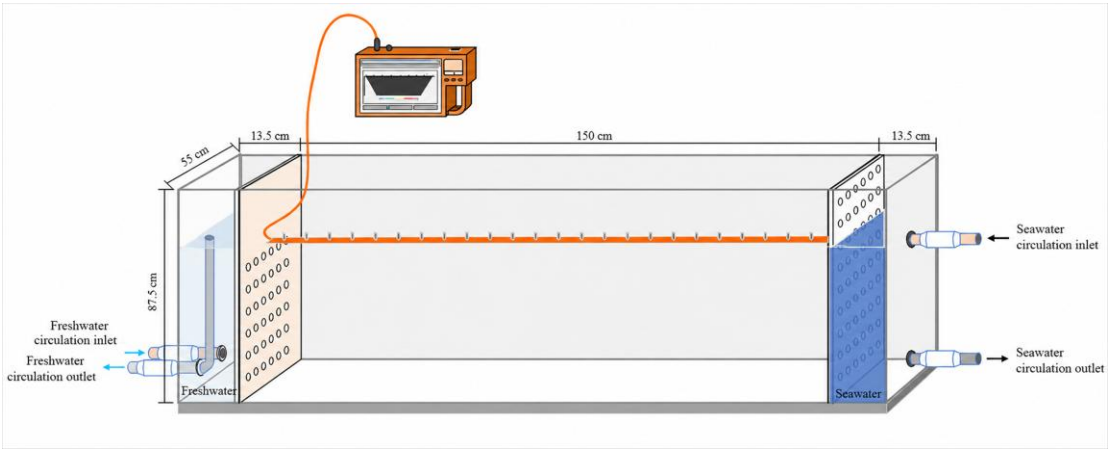


Figure 2. Schematic of the laboratory tank apparatus.

3.2 Conceptualisation of the physical model

The silty soil used in the laboratory experiments simulating water and salt transport

through the seawater intrusion–soil salinisation hazard chain was collected from the coastal area of Laizhou Bay. According to the borehole records shown in Figure 1, the near-surface stratigraphic succession along the coast of Laizhou Bay consists, from top to bottom, of clayey sand, medium-to-fine sand and clayey sand.

Representative sediment samples were collected from the different stratigraphic units in the study area. After collection, the samples were air-dried, crushed, sieved and homogenised in the laboratory. Their basic physicochemical properties were then measured, including particle density, water content, bulk density, void ratio, hydraulic conductivity and particle-size distribution. The measured porosities of the sand layer and silty-soil layers were 0.56 and 0.40, respectively.

To reproduce the soil environment along the coast of Laizhou Bay, the sediments were placed into the experimental tank in successive layers and compacted to ensure uniform porosity and packing density within each layer. The experimental stratigraphy was proportionally scaled from the field setting. The upper silty layer and middle sand layer were each 10 cm thick. Because basal leakage was not considered in the experiment, the lower silty layer, representing a weakly permeable unit, was set to a thickness of 50 cm, and no deeper sandy aquifer was included.

3.3 Experimental design

The laboratory simulations were designed to examine the effects of hydraulic-head difference and stratal slope on water and salt transport within the seawater intrusion–soil salinisation hazard chain. The experimental factor levels were selected to represent the hydraulic gradients and slopes observed under field conditions along the southern coast of Laizhou Bay. A landward hydraulic gradient was imposed by adjusting the water levels in the saltwater and freshwater reservoirs. Hydraulic-head differences (Δh)

206 of 0, 5 and 10 cm were tested, corresponding to hydraulic gradients (i) of 0, 0.033 and
207 0.067, respectively.
208
209 The stratal slope was varied by adjusting the angle of the tilting platform beneath the
210 experimental tank. Two slopes, 0° and 1.5°, were tested.
211

212 3.4 Electrical resistivity monitoring

213 The electrical resistivity tomography (ERT) monitoring system comprised a main
214 measurement unit, a voltage booster and a multielectrode cable connected in sequence.
215 A GeoPen E60DN distributed electrical resistivity instrument was used as the main
216 measurement unit, and measurements were acquired using a Schlumberger array. The
217 acquisition parameters comprised 23 measurement levels, an energisation time of 1 s
218 and a nominal current of 1 A. Resistivity measurements were conducted at 2-h intervals.
219 The stainless-steel electrodes had an external diameter of 3.5 mm and a length of 1 cm.
220 A total of 48 electrodes were installed at 3-cm intervals along the top of the sediment
221 layers in the main tank, following the orientation shown in Figure 2.
222
223 For quality control, a datum was classified as an outlier if it exceeded five times the
224 values of the two neighbouring data points or was less than one fifth of those values.
225 Outliers and measurements acquired with an applied current below 20 mA were
226 removed. The excluded data accounted for less than 1% of the complete dataset. Quality
227 control was performed after data acquisition, and no real-time screening was applied
228 during measurement.
229
230 The apparent-resistivity data were inverted using RES2DINV version 3.50. Before
231 inversion, the data were reformatted into the required column structure, and
232 measurements with anomalous current values were removed. Nonlinear least-squares
233 inversion was then applied, and the result from the fourth iteration was retained for each

dataset. When the root-mean-square (RMS) error was excessively high, the data were further adjusted by removing values with a dispersion greater than 30%. Because very low RMS errors may indicate overfitting and produce resistivity models that do not represent the actual conditions (Dimova et al., 2012), the RMS error of the apparent-resistivity inversions was maintained at approximately 10% in this study.

3.5 Salinity calculation

To determine the spatiotemporal distribution of pore-water salinity within the tank, the bulk resistivity obtained from inversion was treated as the formation resistivity (*Rf*). Relationships between formation resistivity and pore-water resistivity were then established for each sediment type. The top surface of the model was defined as the origin of the vertical coordinate, with the positive z-axis directed upwards. The upper silty layer extended from z = -0.006 to -0.141 m, whereas the underlying sand layer extended from z = -0.166 to -0.296 m. According to the theory of electrical conduction in porous media, the resistivity of saturated sediment depends on pore-water resistivity, porosity and surface-conduction effects.

(1) Pore-water resistivity in the clay-bearing layer

Electrical conductivity is the reciprocal of electrical resistivity. Accordingly, the bulk conductivity (σ_b) and pore-water conductivity (σ_w) are given by:

$$\sigma_b = \frac{1}{R_f}, \sigma_w = \frac{1}{R_w} \tag{1}$$

The Waxman-Smits model accounts for both electrolytic conduction through pore water and surface conduction associated with clay minerals. Its general form is (Waxman and Smits, 1968):

$$\sigma_b = \frac{S_w^{n^*}}{F^*}\left(\sigma_w + \frac{BQ_v}{S_w}\right) \tag{2}$$

where S_w is water saturation; n^* is the equivalent saturation exponent; F^* is the equivalent formation factor corresponding to the total porosity of the clay-bearing

medium; B is the equivalent conductance of exchangeable cations; and Q_v is the cation-exchange capacity per unit pore volume. The sediment layers remained saturated throughout the experiment. Therefore, $S_w = 1$ and $n^* = 1$, and Equation 2 simplifies to:

$$\frac{F^*}{R_f} = \sigma_w + BQ_v \tag{3}$$

The equivalent conductance of exchangeable cations depends on pore-water conductivity and temperature and is expressed as:

$$\begin{aligned} B &= B_{\max}(1 - 0.83e^{-0.5\sigma_w}) \\ B_{\max} &= -1.2879 + 0.2205T - 0.0004T^2 \end{aligned} \tag{4}$$

where T is the pore-water temperature (°C). The cation-exchange capacity of the clay-bearing material was calculated as follows (Li et al., 2012):

$$Q_v = \frac{\mathrm{CEC_{Cl}}\omega_t\rho_s V_s}{100\varphi} \tag{5}$$

where CEC_{Cl} is the mean cation-exchange capacity of the clay minerals; ω_t is the clay mass fraction; ρ_s is sediment particle density; V_s is the unit volume; and φ is porosity. Substitution of the parameters in Table 2 gives $Q_v = 0.06260$ and $B_{max} = 1.3005$. Because B varies with σ_w, pore-water conductivity was obtained by solving the following nonlinear equation:

$$g(\sigma_w) = \sigma_w + B_{\max}(1 - 0.83e^{-0.5\sigma_w})Q_v - \frac{F^*}{R_f} = 0 \tag{6}$$

Equation 6 was solved using the Newton iterative method. After convergence, the pore-water resistivity of the clay-bearing layer was calculated using Equation 1.

(2) Pore-water resistivity in the sand layer

Because the clay content of the sand layer was low, surface conduction by the sediment grains was assumed to be negligible. Archie's law was therefore used to relate formation resistivity to pore-water resistivity (Archie, 1942):

$$F = \frac{a}{\varphi^m} = \frac{R_f}{R_w} \tag{7}$$

where a is the tortuosity coefficient and m is the cementation exponent. Using a sand-

277 layer porosity φ of 0.56, a of 0.6 and m of 1.4 gives a formation factor F of 2.6087.
278 Thus:

$$R_w = \frac{R_f}{F} = \frac{R_f}{2.6087} \tag{8}$$

279 (3) Temperature correction and salinity conversion

280 Electrical resistivity is temperature dependent. The two models above yield pore-
281 water resistivity at the experimental temperature of 12 °C, whereas the empirical
282 salinity relationship uses 75 °F (approximately 23.6 °C) as its reference temperature.
283 Pore-water resistivity was therefore corrected before conversion to salinity using:

$$R_{w,23.6} = R_{w,T}\frac{T + 21.0}{44.89} = 0.73513R_{w,12} \tag{9}$$

284 The corrected pore-water resistivity R_w,23.6 (Ω·m) was substituted into the
285 following piecewise empirical relationship to obtain pore-water salinity C (ppm):

$$C = \begin{cases} \dfrac{3113}{R_{w,23.6}^{1.352}} & , \ R_{w,23.6} \leq 0.10 \\ \dfrac{7000}{R_{w,23.6}} & , \ 0.10 < R_{w,23.6} \leq 0.20 \\ \dfrac{5490}{R_{w,23.6}^{1.151}} & , \ R_{w,23.6} > 0.20 \end{cases} \tag{10}$$

286

287 3.6 Salt storage calculation

288 In this study, salt storage was operationally defined as the mass of dissolved salt in pore
289 water within a fixed soil volume. Each computational unit measured 0.03 m
290 horizontally, 0.10 m vertically and 0.01 m across the tank. In accordance with the
291 experimental discretisation grid, the interval from z = -0.006 to -0.097 m was used to
292 represent the upper 0.10 m soil layer. Each unit had a soil volume V_s of 30 cm^3 and a
293 porosity φ of 0.40. Forty-seven computational positions were defined along the tank,
294 with their horizontal coordinates calculated as follows:

$$X_i = 0.015 + 0.030(i - 1)\, m \tag{11}$$

where X_i is the horizontal coordinate of inversion cell i, and i is the cell number increasing from the seawater boundary towards the freshwater boundary. The mean pore-water salinity at each horizontal position was calculated as:

$$\overline{C}_i = \frac{1}{N_i}\sum_{j=1}^{N_i} C\left(X_i, z_j\right) \tag{12}$$

where $C(X_i, z_j)$ is the pore-water salinity at horizontal position X_i and depth z_j , and N_i is the number of valid depth nodes included at that position.

Assuming complete saturation, the pore-water volume in each computational unit was $Vw = \varphi V_s = 12$ cm^3 = 0.012 L. The numerical salinity value in ppm was treated as mg L^{-1} for the aqueous solution. The dissolved-salt mass in computational unit i was therefore calculated as:

$$M_i = V_s \varphi \overline{C}_i \times 10^{-3} = 0.012\overline{C}_i \text{mg} \tag{13}$$

where M_i is the mass of salt dissolved in the pore water within 30 cm^3 of soil. The M_i values obtained at the 47 horizontal positions describe the longitudinal distribution of dissolved-salt mass along the tank. This metric represents only dissolved salt in the pore water and excludes salt adsorbed on sediment surfaces and any precipitated solid-phase salt.

3.7 Classification of soil salinisation severity

Soil salinisation severity was represented by the dissolved-salt mass in pore water within a fixed volume of the upper silty layer, as calculated using Equation 13.

Soil salinisation severity was classified using the established salt-affected soil classification of Richards (1954). This classification uses the electrical conductivity of the saturation extract (ECe) to distinguish non-salinised, slightly salinised, moderately salinised, severely salinised and extremely salinised soils. These classes were converted into soil-salt-content thresholds using the empirical relationship between soil electrical conductivity and total soluble salt content (Rengasamy, 2010).

For the fixed soil volume defined in Section 3.7, the dry-soil mass corresponding to a 30 cm^3 sample was calculated as:

$$M_d = V(1-\varphi)\rho_s \quad (14)$$

where M_d is dry-soil mass, V is sample volume, φ is porosity and ρ_s is sediment particle density. The dissolved-salt mass within 30 cm^3 of soil was used to assess the severity of soil salinisation induced by seawater intrusion. Thresholds of 39.2, 78.3, 156.7 and 313.3 mg were used to distinguish the salinisation severity classes listed in Table 3.

Table 2. Parameters used for resistivity-to-salinity conversion.

Parameter	Symbol	Value	Applicable medium	Description
Equivalent formation factor	F^*	4.7	Clay-bearing sediment	Saturated conditions
Water saturation	S_w	1.0	Clay-bearing sediment	Fully saturated
Equivalent saturation exponent	n^*	1.0	Clay-bearing sediment	Fully saturated
Temperature	T	12 ℃	Clay-bearing sediment/sand	Experimental temperature
Porosity	φ	0.40	Clay-bearing sediment	Waxman-Smits model
Clay mass fraction	ω_t	0.15	Clay-bearing sediment	Mass fraction
Sediment particle density	ρ_s	1.7 g·cm^{-3}	Clay-bearing sediment	Experimental parameter
Mean cation-exchange capacity of clay minerals	CEC_{Cl}	9.82 meq/100 g	Clay-bearing sediment	Experimental parameter
Porosity	φ	0.56	Sand	Archie's law
Tortuosity coefficient	a	0.6	Sand	Archie coefficient
Cementation exponent	m	1.4	Sand	Archie coefficient

Table 3. Soil salinisation classes and dissolved-salt mass thresholds for a fixed soil volume.

Severity class	Soil salt content ($mg \cdot kg^{-1}$)	Dissolved-salt mass in 30 cm^3 soil (mg)
Non-salinised	<1,280	<39.2
Slightly salinised	1,280-2,560	39.2-78.3
Moderately salinised	2,560-5,120	78.3-156.7
Severely salinised	5,120-10,240	156.7-313.3
Extremely salinised	>10,240	>313.3

4. Results

4.1 Resistivity section

To quantify the electrical changes in different sediment layers during seawater intrusion, the median inverted resistivity of all cells was calculated separately for the upper silty layer and middle sand layer. These median values were used to characterise the overall resistivity of each layer.

At a stratal slope of 0° and a hydraulic-head difference of 0 cm, the median resistivities of the upper silty layer and middle sand layer at 12 h were approximately 48.5 and 107.9 Ω·m, respectively. By 72 h, they had decreased to approximately 9.6 and 14.1 Ω·m, representing reductions of approximately 38.9 and 93.8 Ω·m relative to the 12 h values. At the same hydraulic-head difference but a stratal slope of 1.5°, the corresponding median resistivities were approximately 50.0 and 96.4 Ω·m at 12 h and 12.9 and 82.9 Ω·m at 72 h.

At a stratal slope of 0° and a hydraulic-head difference of5 cm, the median resistivities of the upper silty layer and middle sand layer decreased from approximately 26.6 and 66.0 Ω·m at 12 h to 2.4 and 6.8 Ω·m at 72 h, respectively. When the hydraulic-head difference was increased to 10 cm, the corresponding values decreased from

approximately 49.8 and 60.3 Ω·m to 2.1 and 6.0 Ω·m. As the hydraulic-head difference increased, low-resistivity anomalies appeared earlier, extended farther horizontally and exhibited greater interlayer connectivity (Figure 4). Locally, the anomalies formed patches or narrow bands rather than advancing as a smooth front.

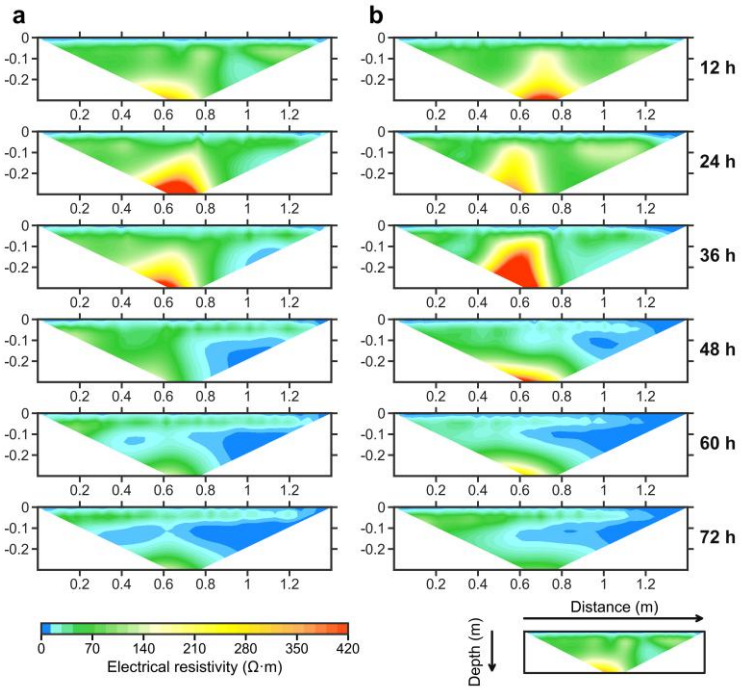


Figure 3. Resistivity sections at different stratal slopes under a hydraulic-head difference of 0 cm: (a) 0° and (b) 1.5°. From left to right, the columns show the results at 12, 24, 36, 48, 60 and 72 h.

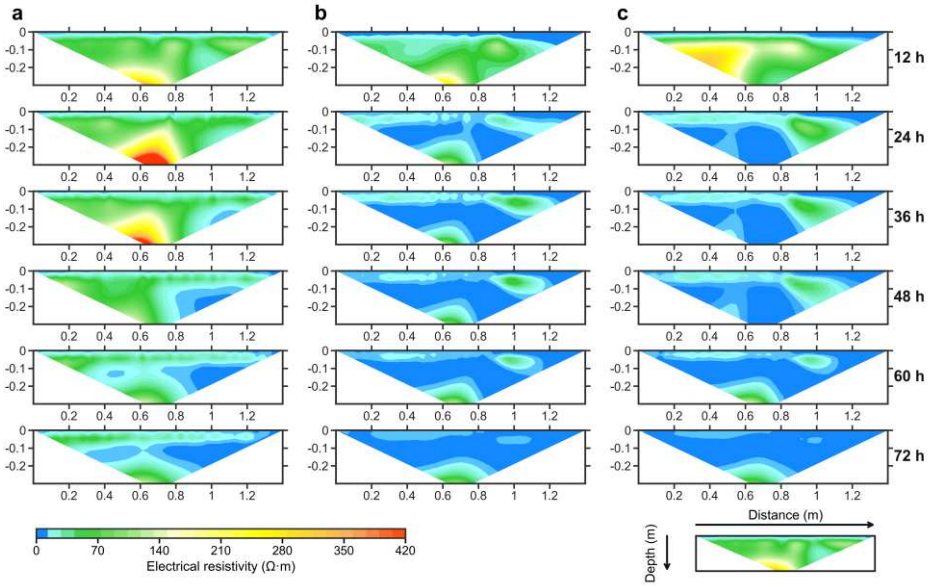


Figure 4. Resistivity sections at different hydraulic-head differences under a stratal slope of 0°: (a) 0 cm, (b) 5 cm and (c) 10 cm. From left to right, the columns show the results at 12, 24, 36, 48, 60 and 72 h, respectively.

4.2 Salinity sections

Following the groundwater salinity classification proposed by the US Geological Survey, pore-water salinity was used to characterise the degree of seawater intrusion (Osborn et al., 2013). Areas with salinities below 1,000 $mg \cdot L^{-1}$ were classified as freshwater zones. Salinities of 1,000–3,000, 3,000–10,000 and 10,000–35,000 $mg \cdot L^{-1}$ represented slightly saline, moderately saline and highly saline intrusion zones, respectively (Figures 7–10).

At a hydraulic-head difference of 0 cm, the salinity field initially maintained a low-salinity background. The high-salinity zone subsequently extended slowly landward from the lower part of the seawater boundary along the sand layer and dispersed upwards into the upper silty layer (Figure 5a). When the hydraulic-head difference increased to 5 cm, high-salinity anomalies (>10,000 $mg \cdot L^{-1}$) appeared earlier. Several localised high-salinity patches and vertically connected zones developed during the intermediate stage and gradually expanded and coalesced during the late stage (Figure 5b). At a hydraulic-head difference of 10 cm, the near-seawater high-salinity zone, an inland high-salinity lens and local vertical high-salinity bands coexisted during the early to intermediate stages. Their horizontal extent and interlayer connectivity increased further during the late stage (Figure 5c). Thus, increasing the hydraulic-head difference was characterised by earlier anomaly development, a broader affected area and intensified interlayer salt transfer. Local salinity maxima did not increase linearly, probably because they were influenced by heterogeneous flow pathways and dispersion.

At a hydraulic-head difference of 0 cm and a stratal slope of 0°, saline water formed a relatively continuous landward-extending band along the sand layer during the late stage and migrated upwards into the upper silty layer (Figure 6a). When the stratal slope increased to 1.5°, continuous extension towards the freshwater boundary became less

pronounced during the late stage. The high-salinity zones were concentrated mainly near the seawater boundary and within local middle-to-lower parts of the profile (Figure 6b).

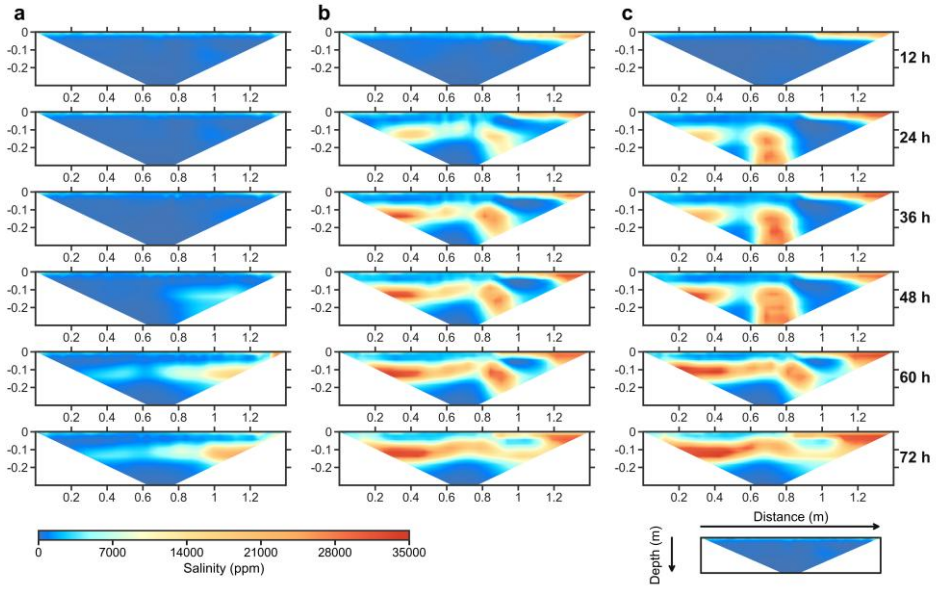


Figure 5. Pore-water salinity sections at different hydraulic-head differences under a stratal slope of 0°: (a) 0 cm, (b) 5 cm and (c) 10 cm. From left to right, the columns show the results at 12, 24, 36, 48, 60 and 72 h.

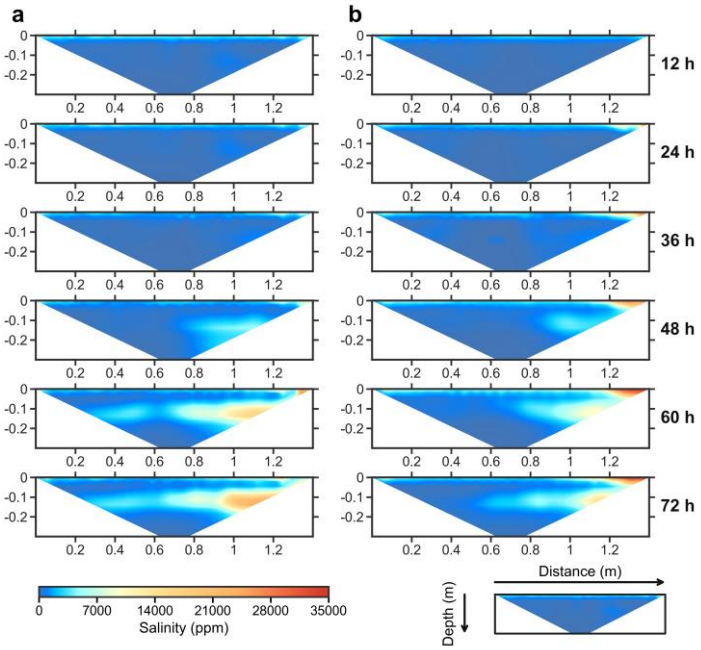


Figure 6. Pore-water salinity sections at different stratal slopes under a hydraulic-head difference of 0 cm: (a) 0° and (b) 1.5°. From left to right, the columns show the results at 12, 24, 36, 48, 60 and 72 h.

4.3 Salt storage results

At a stratal slope of 0° and a hydraulic-head difference of 0 cm, salt storage at S1, S2 and S3 remained largely within the non-salinised range during the first 36 h. At 72 h, the peak values increased to approximately 370, 190 and 180 mg, corresponding to extremely, severely and severely salinised conditions, respectively. When the stratal slope increased to 1.5°, the corresponding peak values at 72 h were approximately 180, 135 and 55 mg. These values represented severely, moderately and slightly salinised conditions, respectively. Salinisation severity at all three locations was lower than under the 0° condition.

At a hydraulic-head difference of 5 cm, the peak salt-storage values at S1, S2 and S3 were approximately 220, 165 and 40 mg at 12 h and 210, 95 and 140 mg at 72 h, respectively. Extremely salinised conditions did not develop during the experiment. At a hydraulic-head difference of 10 cm, the corresponding peak values increased from approximately 120, 95 and 10 mg at 12 h to 335, 180 and 165 mg at 72 h. At this time, S1 reached the extremely salinised class, whereas S2 and S3 reached the severely salinised class. Table 4 summarises the salt-storage values, salinisation severity classes and seawater-intrusion distances at each observation time.

418 **Table 4.** Surface-layer salt storage, soil salinisation classes and seawater-intrusion extent under different experimental conditions

Slope (°) Δh (cm)	Time (h)	S1 salt storage (mg) (salinisation class)	S2 salt storage (mg) (salinisation class)	S3 salt storage (mg) (salinisation class)	Seawater-intrusion class
Slope = 0° Δh = 0 cm	12	<39.2 (Non-salinised)	<39.2 (Non-salinised)	<39.2 (Non-salinised)	Freshwater zone (0 m)
	24	<39.2 (Non-salinised)	<39.2 (Non-salinised)	<39.2 (Non-salinised)	Freshwater zone (0 m)
	36	≈39.2 (Slight)	<39.2 (Non-salinised)	<39.2 (Non-salinised)	Freshwater zone (0 m)
	48	≈85 (Moderate)	≈30 (Non-salinised)	≈60 (Slight)	Highly saline water (approx. 0.10 m)
	60	≈250 (Severe)	≈110 (Moderate)	≈170 (Severe)	Highly saline water (approx. 0.45 m)
	72	≈370 (Extremely severe)	≈190 (Severe)	≈180 (Severe)	Highly saline water (approx. 0.45 m)
Slope = 1.5° Δh = 0 cm	12	<39.2 (Non-salinised)	<39.2 (Non-salinised)	<39.2 (Non-salinised)	Freshwater zone (0 m)
	24	≈135 (Moderate)	≈110 (Moderate)	≈25 (Non-salinised)	Highly saline water (approx. 0.20 m)
	36	≈145 (Moderate)	≈110 (Moderate)	<39.2 (Non-salinised)	Highly saline water (approx. 0.20 m)
	48	≈160 (Severe)	≈125 (Moderate)	<39.2 (Non-salinised)	Highly saline water (approx. 0.25 m)
	60	≈205 (Severe)	≈160 (Severe)	≈50 (Slight)	Highly saline water (approx. 0.25 m)
	72	≈180 (Severe)	≈135 (Moderate)	≈55 (Slight)	Highly saline water (approx. 0.35 m)
Slope = 0° Δh = 5 cm	12	≈220 (Severe)	≈165 (Severe)	≈40 (Slight)	Highly saline water (approx. 0.45 m)
	24	≈145 (Moderate)	≈110 (Moderate)	≈55 (Slight)	Highly saline water (approx. 1.05 m)
	36	≈190 (Severe)	≈135 (Moderate)	≈60 (Slight)	Highly saline water (approx. 1.20 m)
	48	≈230 (Severe)	≈125 (Moderate)	≈100 (Moderate)	Highly saline water (approx. 1.20 m)
	60	≈170 (Severe)	≈95 (Moderate)	≈90 (Moderate)	Highly saline water (approx. 1.25 m)

Slope (°) Δh (cm)	Time (h)	S1 salt storage (mg) (salinisation class)	S2 salt storage (mg) (salinisation class)	S3 salt storage (mg) (salinisation class)	Seawater-intrusion class
Slope = 0° Δh = 10 cm	72	≈210 (Severe)	≈95 (Moderate)	≈140 (Moderate)	Highly saline water (approx. 1.25 m)
	12	≈120 (Moderate)	≈95 (Moderate)	≈10 (Non-salinised)	Highly saline water (approx. 0.45 m)
	24	≈210 (Severe)	≈160 (Severe)	≈55 (Slight)	Highly saline water (approx. 1.15 m)
	36	≈230 (Severe)	≈160 (Severe)	≈60 (Slight)	Highly saline water (approx. 1.20 m)
	48	≈220 (Severe)	≈160 (Severe)	≈95 (Moderate)	Highly saline water (approx. 1.25 m)
	60	≈300 (Severe)	≈185 (Severe)	≈165 (Severe)	Highly saline water (approx. 1.25 m)
	72	≈335 (Extremely severe)	≈180 (Severe)	≈165 (Severe)	Highly saline water (approx. 1.30 m)

Note: S1, S2 and S3 denote pore-water salt storage in the entire 30 cm^3 soil volume, the lower 15 cm^3 volume and the upper 15 cm^3 volume, respectively. The seawater-intrusion class was defined as the highest salinity class observed in each profile at each observation time. Values in parentheses give the horizontal distance from the seawater boundary (x = 1.40 m) to the most landward position of the corresponding salinity contour. The freshwater zone had a pore-water salinity below 1,000 mg L^{-1}, and its intrusion distance was recorded as 0 m.

5. Discussion

5.1 Effects of hydraulic-head difference and stratal slope on seawater intrusion rates

At a hydraulic-head difference of 0 cm, the entire section remained within the freshwater range during the first 36 h. Highly saline water appeared only at approximately 48 h, and its intrusion distance reached approximately 0.45 m at 72 h. When the hydraulic-head difference increased to 5 and 10 cm, highly saline water was already present at 12 h, and its intrusion distance reached approximately 1.25 and 1.30 m, respectively, at 72 h (Figures 7, 9 & 10). A larger hydraulic-head difference enabled saline water to enter the sand layer and migrate towards the freshwater boundary more rapidly, followed by salt dispersion into the silty layers. This result is consistent with previous tank experiments showing that the boundary water-level difference controls the response time and advance rate of the saltwater wedge (Goswami and Clement, 2007; Yu et al., 2019).

In this experiment, the maximum salinity at some observation points did not increase with increasing hydraulic-head difference. This finding indicates that the intrusion rate and local salinity response were also affected by preferential pathways, dispersion and salt redistribution. Assessments of hydraulic-head effects should therefore focus on the onset and overall spatial extent of high-salinity zones rather than the maximum value at an individual observation point.

The layered sedimentary structure was an important cause of the heterogeneous salinity distribution. The relatively permeable middle sand layer provided the principal pathway for horizontal saltwater transport. By contrast, the upper and lower silty layers had lower permeability and slowed saltwater advance. Nevertheless, salt transfer into the upper silty layer promoted soil salinisation. Previous studies of heterogeneous aquifers

have similarly shown that high-permeability pathways and low-permeability barriers jointly modify the position of the saltwater wedge and the width of the mixing zone (Ahmed et al., 2022). Compared with homogeneous tank models, the present experiment more closely reproduced the interbedded sand and silt deposits of Laizhou Bay. This stratified configuration also explains the coexistence of high-salinity lenses and local salinity peaks and troughs.

Increasing the stratal slope primarily restricted the landward advance of the low- to moderate-salinity fronts during the intermediate and late stages. At 72 h, the intrusion distances of slightly saline, moderately saline and highly saline water were approximately 1.20, 1.10 and 0.45 m, respectively, under the 0° condition. Under the 1.5° condition, the corresponding distances were approximately 0.95, 0.75 and 0.35 m (Figures 7 & 8). Thus, within the present experimental configuration, increasing the stratal slope from 0° to 1.5° inhibited seawater intrusion. Previous studies have shown that the effect of slope also depends on aquifer thickness, dip direction and boundary conditions (Shi et al., 2020). The present results therefore demonstrate only that a 1.5° slope weakened late-stage landward expansion under the tested stratigraphic and hydrodynamic conditions; they should not be interpreted as evidence that seawater intrusion necessarily decreases monotonically with increasing slope.

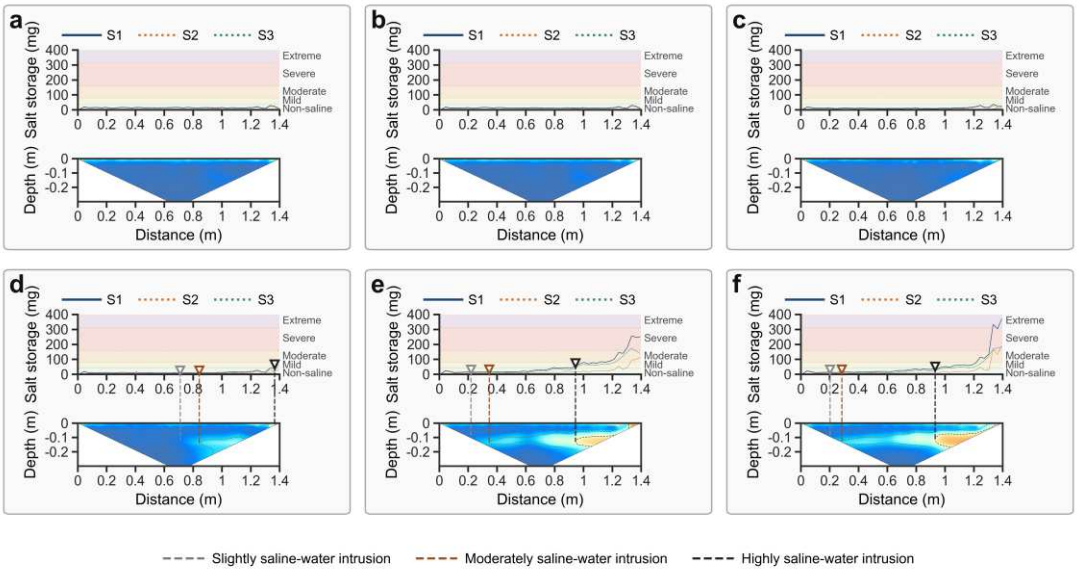


Figure 7. Surface-layer salt storage and salinity-classified extents of seawater intrusion at a stratal slope of 0° and a hydraulic-head difference of 0 cm. Panels (a–f) show the results at 12, 24, 36, 48, 60 and 72 h, respectively. S1, S2 and S3 denote the salt-storage curves for the entire 30 cm^3 soil section, the lower 15 cm^3 section and the upper 15 cm^3 section, respectively. The grey, brown and black dashed lines indicate the boundaries of slightly saline, moderately saline and highly saline water intrusion, respectively.

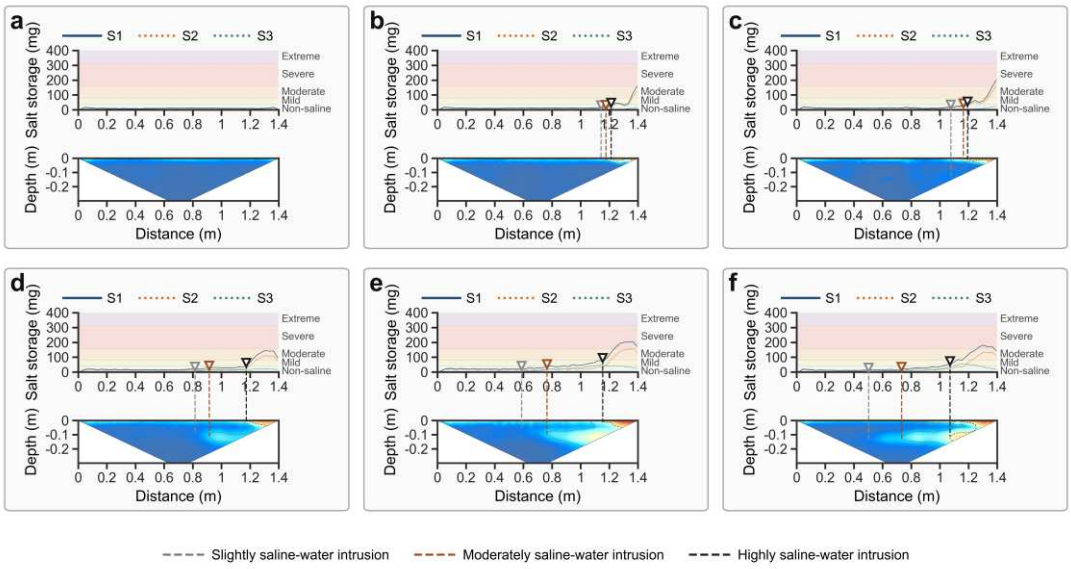


Figure 8. Surface-layer salt storage and salinity-classified extents of seawater intrusion at a stratal slope of 1.5° and a hydraulic-head difference of 0 cm. Panels (a–f) show the results at 12, 24, 36, 48, 60 and 72 h, respectively. S1, S2 and S3 denote the salt-storage curves for the entire 30 cm^3

soil section, the lower 15 cm^3 section and the upper 15 cm^3 section, respectively. The grey, brown and black dashed lines indicate the boundaries of slightly saline, moderately saline and highly saline water intrusion, respectively.

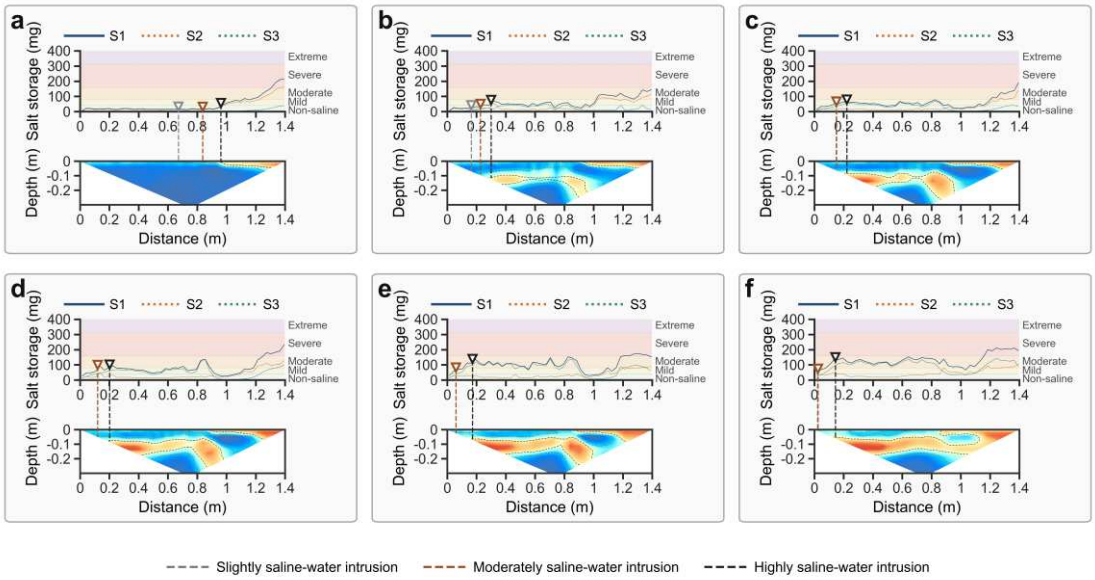


Figure 9. Surface-layer salt storage and salinity-classified extents of seawater intrusion at a stratal slope of 0° and a hydraulic-head difference of 5 cm. Panels (a–f) show the results at 12, 24, 36, 48, 60 and 72 h, respectively. S1, S2 and S3 denote the salt-storage curves for the entire 30 cm^3 soil section, the lower 15 cm^3 section and the upper 15 cm^3 section, respectively. The grey, brown and black dashed lines indicate the boundaries of slightly saline, moderately saline and highly saline water intrusion, respectively.

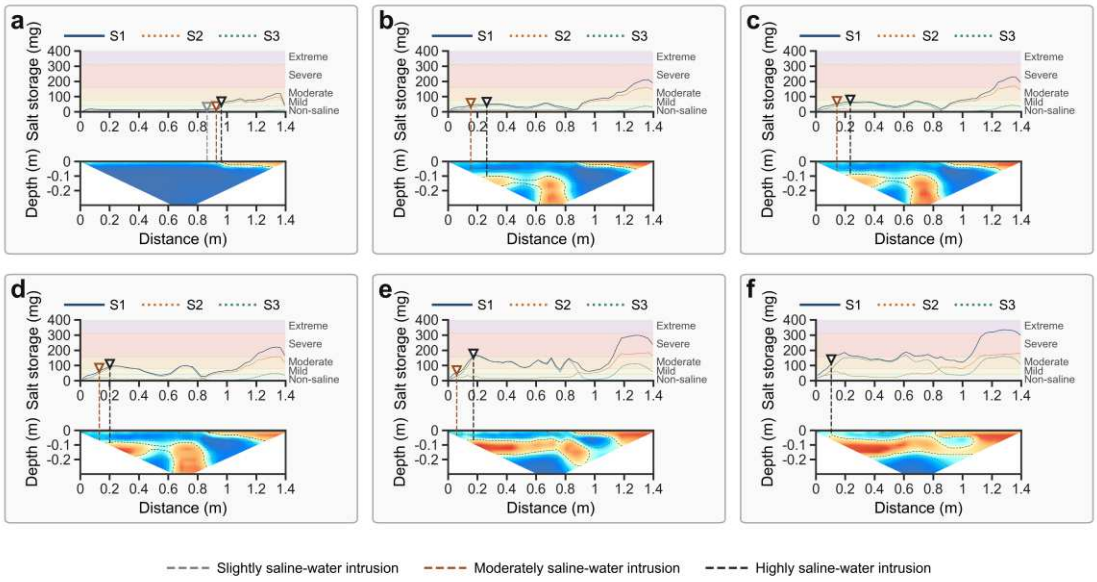


Figure 10. Surface-layer salt storage and salinity-classified extents of seawater intrusion at a stratal slope of 0° and a hydraulic-head difference of 10 cm. Panels (a–f) show the results at 12, 24, 36, 48, 60 and 72 h, respectively. S1, S2 and S3 denote the salt-storage curves for the entire 30 cm^3 soil section, the lower 15 cm^3 section and the upper 15 cm^3 section, respectively. The grey, brown and black dashed lines indicate the boundaries of slightly saline, moderately saline and highly saline water intrusion, respectively.

5.2 Effects of hydraulic-head difference and stratal slope on the evolution of soil salinisation

The salt-storage results further demonstrate that seawater intrusion and surface-layer salinisation were broadly related but exhibited a measurable time lag. At a stratal slope of 0° and Δh = 0 cm, the upper silty layer remained predominantly non-salinised during the first 36 h despite the formation of a deep high-salinity zone. The S1 section on the seaward side reached the extremely severe salinisation level only at 72 h (Figure 7). At a stratal slope of 1.5° and Δh = 0 cm, the seaward side reached the severe salinisation level earlier, but no extremely severe salinisation zone comparable to that under the 0° condition developed within 72 h (Figure 8). As the hydraulic-head difference increased, S1 crossed the salinisation thresholds earlier, accompanied by increases in S2 and S3

(Figures 7, 9 & 10).

Previous studies have similarly shown that changes in shallow-layer salinisation, the saltwater-wedge front and the total salt mass within an aquifer are not always synchronous (Badaruddin et al., 2015). The observed time lag primarily arose from a two-stage transport process. First, saltwater migrated rapidly landwards through the sand layer. Second, salt crossed the sand–silt interface, entered the shallow layer and gradually accumulated within the low-permeability silty sediment. Increasing the hydraulic-head difference accelerated both stages, resulting in an earlier onset and a greater spatial extent of soil salinisation. Increasing the stratal slope caused more salt to remain concentrated on the seaward side, leading to shallow-layer salinisation during the early stage. Overall, however, the increased slope slowed both transport stages, resulting in a smaller extent of salinisation within the upper silty layer during the intermediate and late stages.

These findings are broadly consistent with field observations from Laizhou Bay. Field monitoring and numerical simulations have shown that high-permeability zones and biogenic conduits can act as preferential pathways for salt transport, while salt in some tidal-flat environments is preferentially retained near the top of the silt cover (Xiao et al., 2024; Zhang et al., 2025). Nevertheless, the present experiment was conducted under continuously saturated conditions and did not account for tidal fluctuations, evaporation, rainfall or capillary rise. These natural processes may further enhance or modify salt accumulation in the surface layer. Moreover, the salt-storage metric used here represents only the dissolved salt in the pore water within 30 cm^3 of soil and excludes adsorbed and crystallised salts. This metric is therefore suitable for comparing the immediate risk of salinity damage among experimental conditions but should not be interpreted as equivalent to the total salt content of natural soils.

5.3 Potential effects of other factors on seawater intrusion and soil salinisation

In addition to stratal slope and hydraulic-head difference, stratigraphic architecture and sediment heterogeneity are key controls on the extent and advance rate of seawater intrusion. The hydraulic conductivity, thickness and lateral continuity of the sand layer, together with its hydraulic connectivity to the silty layers, determine the preferential pathways of saltwater intrusion. High-permeability pathways can accelerate the landward migration of saltwater and widen the mixing zone. By contrast, low-permeability silty layers can retard horizontal transport while promoting the long-term retention of salt that has entered the shallow sediments. Variations in interbed thickness, permeability contrast and the development of local preferential pathways may therefore cause the saltwater front to exhibit localised breakthroughs, lens-shaped accumulation or discontinuous expansion rather than uniform migration (Yu and Michael, 2019; Ahmed et al., 2022).

External hydrological and meteorological conditions can also modify the freshwater–saltwater interface. Rainfall and groundwater recharge from the landward boundary can enhance the seaward discharge of freshwater and reduce pore-water salinity. Groundwater abstraction, by contrast, lowers the landward hydraulic head and increases the landward hydraulic gradient, thereby accelerating seawater intrusion and expanding its spatial extent. In surface soils, evaporation and capillary rise can continuously transport salt from shallow groundwater to the ground surface, leading to salt accumulation. Intense rainfall may temporarily reduce surface-layer salt storage through infiltration and leaching. Consequently, a similar extent of deep seawater intrusion does not necessarily correspond to a similar degree of surface-soil salinisation. Differences in tidal forcing, groundwater recharge and evaporation may still produce markedly different surface-salinity distributions.

6. Conclusion

This study used a laboratory tank containing layered sediments to convert inverted electrical-resistivity data into pore-water salinity and subsequently calculate dissolved-salt storage within a fixed soil volume of 30 cm^3. The effects of hydraulic-head difference and stratal slope on water and salt transport along the seawater intrusion–soil salinisation hazard chain in a layered silty-coast system were systematically investigated. The principal conclusions are as follows.

(1) Saltwater preferentially migrated towards the freshwater boundary through the middle sand layer and subsequently affected the upper silty layer through interlayer exchange. The salinity field evolved from localised anomalies on the seaward side into a continuous intrusion zone, exhibiting a distinctly channelised and stage-dependent pattern rather than uniform advance.

(2) When the hydraulic-head difference increased from 0 to 5 and 10 cm, high-salinity anomalies developed earlier, while their horizontal extent and the hydraulic connectivity between layers increased. The principal effect of a greater hydraulic-head difference was to extend the duration and spatial coverage of higher salinisation classes. Local salinity maxima, however, did not vary monotonically because of heterogeneous transport.

(3) Increasing the stratal slope from 0° to 1.5° generally reduced the landward expansion of the continuous deep high-salinity zone. At 72 h, the intrusion distances of slightly saline, moderately saline and highly saline water were approximately 1.20, 1.10 and 0.45 m, respectively, under the 0° condition, compared with approximately 0.95, 0.75 and 0.25 m under the 1.5° condition. These results demonstrate that, under the tested conditions, increasing the stratal slope inhibited the horizontal advance of seawater.

(4) The successive crossing of salt-storage thresholds further confirmed the progressive spatiotemporal relationship between seawater intrusion and soil salinisation. A marked increase in surface-layer salt storage generally lagged behind the formation of the underlying high-salinity zone. A greater hydraulic-head difference caused the thresholds for slight, moderate, severe and extremely severe salinisation to be crossed earlier and expanded the extent of the higher salinisation classes. During the late stage of the experiment with a hydraulic-head difference of 10 cm, S1 on the seaward side reached the extremely severe salinisation level. This finding indicates that stronger hydraulic forcing can transform localised salt accumulation into a more extensive shallow-layer salinity hazard.

Data Availability Statement

The data used in this study were primarily obtained from laboratory experiments. The resulting datasets are available from the corresponding author upon reasonable request.

Acknowledgements

This work was supported by the National Natural Science Foundation of China (grant number 42276226), the Open Project Program of Shandong Engineering Research Center for Environmental Protection and Remediation of Groundwater (801KF2021-14), and the Deep Earth Probe and Mineral Resources Exploration-National Science and Technology Major Project (2024ZD1004103). The authors gratefully acknowledge the Laizhou Bay Seawater Intrusion and Soil Salinization Field Scientific Observation and Research Station of the Ministry of Natural Resources for its support during field investigation and laboratory work.

References

Abliz, A., Tiyip, T., Ghulam, A., Halik, Ü., Ding, J., Sawut, M., Zhang, F., Nurmemet, I., and Abliz, A. (2016). Effects of shallow groundwater table and salinity on soil salt dynamics in the Keriya Oasis, northwestern China. *Environmental Earth Sciences*, 75, 260. https://doi.org/10.1007/s12665-015-4794-8.

Ahmed, A., Robinson, G., Hamill, G., and Etsias, G. (2022). Seawater intrusion in extremely heterogeneous laboratory-scale aquifer: Steady-state results. *Water*, 14(7), 1069. https://doi.org/10.3390/w14071069.

Archie, G. E. (1942). The electrical resistivity log as an aid in determining some reservoir characteristics. *Transactions of the AIME*, 146(1), 54–62. https://doi.org/10.2118/942054-G.

Badaruddin, S., Werner, A. D., and Morgan, L. K. (2015). Water table salinization due to seawater intrusion. *Water Resources Research*, 51, 8397–8408. https://doi.org/10.1002/2015WR017098.

Beaujean, J., Nguyen, F., Kemna, A., Antonsson, A. V., and Engesgaard, P. (2014). Calibration of seawater intrusion models: Inverse parameter estimation using surface electrical resistivity tomography and borehole data. *Water Resources Research*, 50(8), 6828–6849. https://doi.org/10.1002/2013WR014020.

Comte, J.C., and Banton, O. (2007). Cross-validation of geo-electrical and hydrogeological models to evaluate seawater intrusion in coastal aquifers. *Geophysical Research Letters*, 34(10), L10402. https://doi.org/10.1029/2007GL029981.

Cooper, H. H., Jr., Kohout, F. A., Henry, H. R., and Glover, R. E. (1964). Sea Water in Coastal Aquifers. U.S. Geological Survey Water-Supply Paper 1613-C. https://doi.org/10.3133/wsp1613C.

Dimova, N. T., Swarzenski, P. W., Dulaiova, H., and Glenn, C. R. (2012). Utilizing multichannel electrical resistivity methods to examine the dynamics of the fresh water–seawater interface in two Hawaiian groundwater systems. *Journal of Geophysical Research: Oceans*, 117(C2), C02012. https://doi.org/10.1029/2011JC007509.

Gao, M., Hou, G., and Guo, F. (2016). Conceptual model of underground brine formation in the silty coast of Laizhou Bay, Bohai Sea, China. *Journal of Coastal Research*, 74, 157–165. https://doi.org/10.2112/SI74-015.1.

Glover, R. E. (1959). The pattern of fresh-water flow in a coastal aquifer. *Journal of Geophysical Research*, 64(4), 457–459. https://doi.org/10.1029/JZ064i004p00457.

Goswami, R. R., and Clement, T. P. (2007). Laboratory-scale investigation of saltwater intrusion dynamics. *Water Resources Research*, 43(4), W04418. https://doi.org/10.1029/2006WR005151.

Guo, L. F. (2019). Experimental study of seawater intrusion migration based on electrical resistivity tomography [Master's thesis, Shandong Agricultural University] (in Chinese).

Han, J. L., Wu, S. R., and Wang, H. B. (2007). Preliminary study on geological hazard chains. *Earth Science Frontiers*, 14(6), 11–20 (in Chinese).

He, Y. H. (2016). Research and application of high-density electrical resistivity method in seawater intrusion investigation in Laizhou Bay. *Marine Environmental Science*, 35(2), 301–305 (in Chinese).

Hopfensperger, K. N., Burgin, A. J., Schoepfer, V. A., and Helton, A. M. (2014). Impacts of saltwater incursion on plant communities, anaerobic microbial metabolism, and resulting relationships in a restored freshwater wetland. *Ecosystems*, 17(5), 792–807. https://doi.org/10.1007/s10021-014-9760-x.

Hu, S. J., and Tian, C. Y. (2000). A study of soil-moisture monitoring using a neutron probe. *Agricultural Research in the Arid Areas*, 18(2), 70–75 (in Chinese).

Ibrakhimov, M., Khamzina, A., Forkutsa, I., Paluasheva, G., Lamers, J. P. A., Tischbein, B., Vlek, P. L. G., and Martius, C. (2007). Groundwater table and salinity: Spatial and temporal distribution and influence on soil salinization in Khorezm region (Uzbekistan, Aral Sea Basin). *Irrigation and Drainage Systems*, 21, 219–236. https://doi.org/10.1007/s10795-007-9033-3.

Kazakis, N., Pavlou, A., Vargemezis, G., Voudouris, K. S., Soulios, G., Pliakas, F., and Tsokas, G. (2016). Seawater intrusion mapping using electrical resistivity tomography and hydrochemical data: An application in the coastal area of eastern Thermaikos Gulf, Greece. *Science of the Total Environment*, 543, 373–387. https://doi.org/10.1016/j.scitotenv.2015.11.041.

Kooi, H., Groen, J., and Leijnse, A. (2000). Modes of seawater intrusion during transgressions. *Water Resources Research*, 36(12), 3581–3589. https://doi.org/10.1029/2000WR900243.

Li, Q. F. (2018). Soil salinization characteristics in typical estuarine areas of Jiaozhou Bay and leaching of salts from aquaculture pond soils [Master's thesis, Qingdao University] (in Chinese).

Li, S., Huang, Z., Du, R., et al. (2012). Computational methods for parameters B and Qv in the Waxman–Smits model. *Well Logging Technology*, 36(3), 244–249 https://doi.org/10.3969/j.issn.1004-1338.2012.03.006 (in Chinese).

Li, Y. Y., Li, W. C., and Wang, J. (2022). Research progress on soil water and salt transport based on bibliometric analysis. *Water Saving Irrigation*, 2022(4), 8–15 (in Chinese).

Neubauer, S. C. (2013). Ecosystem responses of a tidal freshwater marsh experiencing saltwater intrusion and altered hydrology. *Estuaries and Coasts*, 36, 491–507. https://doi.org/10.1007/s12237-011-9455-x.

Oiro, S., and Comte, J.-C. (2019). Drivers, patterns and velocity of saltwater intrusion in a stressed aquifer of the East African coast: Joint analysis of groundwater and geophysical data in southern Kenya. *Journal of African Earth Sciences*, 149, 334–347. https://doi.org/10.1016/j.jafrearsci.2018.08.016.

Osborn, N. I., Smith, S. J., and Seger, C. H. (2013). Hydrogeology, Distribution, and Volume of Saline Groundwater in the Southern Midcontinent and Adjacent Areas of the United States. U.S. Geological Survey Scientific Investigations Report 2013-5017. https://doi.org/10.3133/sir20135017.

Ouhamdouch, S., Bahir, M., and Carreira, P. M. (2017). Geochemical and isotopic tools to decipher the origin of mineralization of the coastal aquifer of Essaouira Basin, Morocco. *Procedia Earth and Planetary Science*, 17, 73–76. https://doi.org/10.1016/S1878-5220(17)30063-2.

Qi, C., Xiong, G. Y., Li, C. Z., Fu, Y. S., Zhang, Y. F., Dong, M. X., Fu, T. F., and Li, B. (2023). Simulation of water and salt transport in a seawater intrusion–soil salinization hazard chain on a muddy coast. *Transactions of Oceanology and Limnology* (in Chinese).

Rengasamy, P. (2010). Soil processes affecting crop production in salt-affected soils. *Functional Plant Biology*, 37(7), 613–620. https://doi.org/10.1071/FP09249.

Richards, L. A. (Ed.). (1954). *Diagnosis and Improvement of Saline and Alkali Soils*. Agriculture Handbook No. 60. U.S. Department of Agriculture, Washington, DC.

Salama, R. B., Otto, C. J., and Fitzpatrick, R. W. (1999). Contributions of groundwater conditions to soil and water salinization. *Hydrogeology Journal*, 7(1), 46–64. https://doi.org/10.1007/s100400050179.

Salehin, M., Chowdhury, M. M. A., Clarke, D., Mondal, M. S., Nowreen, S., Jahiruddin, M., and Haque, A. (2018). Mechanisms and drivers of soil salinity in coastal Bangladesh. In R. Nicholls, C. Hutton, W. Adger, S. Hanson, M. Rahman, and M. Salehin (Eds.), Ecosystem Services for Well-Being in Deltas (pp. 333–347). Palgrave Macmillan. https://doi.org/10.1007/978-3-319-71093-8_18.

Shi, W., Lu, C., and Werner, A. D. (2020). Assessment of the impact of sea-level rise on seawater intrusion in sloping confined coastal aquifers. *Journal of Hydrology*, 586, 124872. https://doi.org/10.1016/j.jhydrol.2020.124872.

Steyl, G., and Dennis, I. (2010). Review of coastal-area aquifers in Africa. *Hydrogeology Journal*, 18(1), 217–225. https://doi.org/10.1007/s10040-009-0545-9.

Stigter, T. Y., Nunes, J. P., Pisani, B., et al. (2014). Comparative assessment of climate change and its impacts on three coastal aquifers in the Mediterranean. *Regional Environmental Change*, 14(Suppl. 1), 41–56. https://doi.org/10.1007/s10113-012-0377-3.

Sun, Q., Gao, M., Wen, Z., Guo, F., Hou, G., Liu, Z., et al. (2023a). Reactive transport modeling for the effect of pumping activities on the groundwater environment in muddy coasts. Journal of Hydrology, 621, 129614. https://doi.org/10.1016/j.jhydrol.2023.129614yl

Thorn, P., and Urish, D. (2013). Preliminary observation of complex salt-fresh water mixing in a beach aquifer. *Groundwater*, 51(1), 145–150. https://doi.org/10.1111/j.1745-6584.2012.00947.x.

Tong, X. (2015). Monitoring saltwater intrusion in the Dagu River using electrical resistivity methods [Master's thesis, Ocean University of China] (in Chinese).

Vallejos, A., Sola, F., and Pulido-Bosch, A. (2015). Processes influencing groundwater level and the freshwater–saltwater interface in a coastal aquifer. *Water Resources Management*, 29(3), 679–697. https://doi.org/10.1007/s11269-014-0621-3.

Wang, Y. X. (2020). Hydrogeochemical processes during seawater intrusion in Longkou, Shandong Province [Master's thesis, China University of Geosciences (Beijing)] (in Chinese).

Wang, Y., Xiao, D., Li, Y., and Li, X. (2008). Soil salinity evolution and its relationship with dynamics of groundwater in the oasis of inland river basins: Case study from the Fubei region of Xinjiang Province, China. *Environmental Monitoring and Assessment*, 140(1–3), 291–302. https://doi.org/10.1007/s10661-007-9867-z.

Wang, Z. Q., Zhu, S. Q., and Yu, R. P. (1993). Saline and Alkali Soils of China. Science Press (in Chinese).

Waxman, M. H., and Smits, L. J. M. (1968). Electrical conductivities in oil-bearing shaly sands. *Society of Petroleum Engineers Journal*, 8(2), 107–122. https://doi.org/10.2118/1863-A.

Xiao, X., Zhang, Y., Fu, T., Sun, Z., Lei, B., Li, M., and Guo, X. (2024). The two salinity peaks mode of marine salt supply to coastal underground brine during a single tidal cycle. *Frontiers in Marine Science*, 10, 1324163. https://doi.org/10.3389/fmars.2023.1324163.

Xu, X. Y., Fu, T. F., Xiong, G. Y., Su, Q., Liu, W. Q., and Chen, G. Q. (2020). A preliminary study of the seawater intrusion–soil salinization hazard chain. *Advances in Marine Science*, 38(1), 1–10 (in Chinese).

Yao, R. J., Yang, J. S., and Jiang, L. (2007). Spatial variability of soil salinity and reasonable sampling number in the Yellow River Delta. *Journal of Soil and Water Conservation*, 20(6), 89–94 (in Chinese).

Yu, X., and Michael, H. A. (2019). Mechanisms, configuration typology, and vulnerability of pumping-induced seawater intrusion in heterogeneous aquifers. *Advances in Water Resources*, 128, 117–128. https://doi.org/10.1016/j.advwatres.2019.04.013.

Yu, X., Xin, P., and Lu, C. (2019). Seawater intrusion and retreat in tidally affected unconfined aquifers: Laboratory experiments and numerical simulations. *Advances in Water Resources*, 132, 103393. https://doi.org/10.1016/j.advwatres.2019.103393.

Zhang, H. Q. (2021). Assessment of seawater intrusion and vulnerability in a coastal area [Master's thesis, Qingdao University of Technology] (in Chinese).

Zhang, Y. F. (2025). Salinity Circulation and Brine Resource Evolution in the Muddy Tidal Flats of Laizhou Bay Driven by a Salt Pump [Doctoral dissertation, Ocean University of China] (in Chinese).

Zhang, Y., Zheng, T., Guo, X., and Luo, J. (2025). Fate of underground brine resources in beach and neritic zones in shallow aquifers driven by salt pumps. *Water Resources Research*, 61, e2025WR040081. https://doi.org/10.1029/2025WR040081.